Imperial College London

DEPARTMENT OF AERONAUTICS

2019 - 2020 GROUP DESIGN PROJECT

WHOLLY REUSABLE LAUNCH SYSTEM

LAUNCH SYSTEM TEAM

Engine Sizing, Nozzle Design & Attitude Control Systems

Academic supervisor:	Professor Silvestre Pinho
Team:	Propulsion
Student:	Kieran NJ Jones-Tett
Course:	Aeronautics with Spacecraft Engineering
CID:	01349514
Date:	15/06/2020

Abstract

A method for engine sizing has been developed and tested on known engines. It determined an optimal chamber pressure of 5.3MPa and expansion ratio of 15 and 115 for the first and second stage respectively. A detailed nozzle design has also been carried out. The nozzle efficiencies are 99.8% and 99.6% for the lower and upper stage respectively. The lengths and exit diameters are 53cm and 26cm for the lower stage, and 104cm and 71cm for the upper stage. The nozzle will be made from Copper, INCONEL 600 and a Niobium alloy due to a wide range of requirements it must meet. A weight estimate gives a lower stage nozzle mass of 5.4kg and an upper stage nozzle mass of 11.1kg. A TVC system has also been designed using COTS linear actuators. Finally, an RCS system to provide control when the engine is not active has been designed to give a thrust of 450N at a chamber pressure of 150 bar.

Contents

List of Figures

List of Tables

Nomenclature

α Mach Angle

$\dot{m}$ Mass Flow Rate

γ Ratio of Specific Heats

μ Mach Angle

ϕ Characteristic Line Angle

ρ Density

ρ_e Nozzle Exit Radius of Curvature

ρ_i Inlet Radius of Curvature

θ Flow Angle

θ_e Nozzle Exit Angle

θ_i Nozzle Inlet Angle

A Throat Area

c_f Thrust Coefficient

F Thrust

g_e Earth Gravitational Constant

h_g Convective Heat Flux Coefficient

I_{sp} Specific Impulse

M Mach Number

m Molecular Weight

P_a Ambient Pressure

P_c Chamber Pressure

P_e Exit Pressure

R Universal Gas Constant

R_c Combustion Chamber Radius

R_t Nozzle Throat Radius

T_c Combustion Chamber Temperature

u Horizontal Mach Number Perturbation

V Flow Velocity

1 Introduction

A wholly reusable rocket will significantly reduce the costs on getting to space. On current systems, fuel costs make up a tiny fraction of total launch cost, and as such represent the floor of launcher pricing. A reusable rocket designed for small payloads fulfills a key gap in the market as the current option for small satellite producers is to 'piggyback' on a large launch vehicle[1]. This leads to lack of control over schedule and orbital insertion[1]. A rocket designed to be reusable must also necessitate the use of a reusable rocket engine. This requirement is one of the hardest to be met as the temperatures and pressures that take place inside a rocket engine often lead to short component life. No suitable commercial off the shelf engines are available, firstly the reusable requirement limits the choice to a small subset of engines such as the RS-25[2] and SpaceX Merlin[3]. With the added size constraint all available engines become unsuitable, being far too powerful.

The MANTIS engine is the solution to this. The ethos has been to design a minimum part, fully modular engine. This ethos has been the cornerstone of many decisions made including manufacturing, engine cycle and fuel choice. At the crux a modular engine design would allow for components to be removed, refurbished at their own rate and replaced as needed, maximising overall engine lifetime and reducing the lead time on launches. This report should be read in tandem with references [4], [5] & [6] as they provide detail into other engine design choices. In this document overall engine sizing will be accomplished, followed by a detailed design of the engine nozzle, and then the design of attitude control systems.

2 Engine Sizing

Initial engine sizing was needed to determine first approximations for the chamber pressure and expansion ratio based off launch vehicle thrust requirements. In this section a model is built to see how changing the engine parameters impacts the launch vehicle. Then a method of devising the optimal engine parameters from launch vehicle requirements is given.

Reference [7] gives four equations relating I_{sp}, mass flow rate, thrust & thrust coefficient to the properties of the fuel, and the conditions in the combustion chamber. Equations 1a, 1b, 1c & 1d describes these relations.

$$F_e = P_c A^* \{ \frac{2\gamma^2}{\gamma - 1} (\frac{2}{\gamma - 1})^{\frac{\gamma+1}{\gamma-1}} (1 - (\frac{P_e}{P_c})^{\frac{\gamma-1}{\gamma}}) \}^{\frac{1}{2}} \tag{1a}$$
$$+ A_e(P_e - P_a)$$

$$\dot{m} = P_c A^* \{ \gamma (\frac{2}{\gamma + 1})^{\frac{\gamma+1}{\gamma-1}} \frac{m}{RT_c} \}^{\frac{1}{2}} \tag{1b}$$

$$I_{sp} = \frac{F_e}{\dot{m} g_e} \tag{1c}$$

$$c_f = \frac{F_e}{P_c A_t} \tag{1d}$$

The chamber pressure and nozzle expansion ratio are varied to see the impact on engine parameters. Three different fuels are considered. These influence the combustion chamber temperature, molecular weight & specific heat ratio. The chemical properties of the fuels considered is outlined in table 1. Several assumptions were made in the model. Firs, assume the chemical properties of the fuels remain the same, these properties are a weak function of chamber pressure. The temperature in the combustion chamber is also assumed to be equivalent to the adiabatic temperature and that no losses occurred through the nozzle. Finally it is assumed that the flow is stationary in the chamber, meaning the temperature and pressure are the absolute values.

Table 1: Properties of Different Fuels (LOX as oxidiser)

	γ	T_c (K)	M (moles)
Hydrogen[8]	1.20	3500	12.50
Methane[9]	1.21	3953	19.6
Kerosene[10]	1.24	3600	23.4

Figure 2 gives the variation of the four parameters with respect to nozzle expansion ratio for a chamber pressure of 5.3MPa at sea level ambient conditions with a constant exit diameter. Figure 3 shows the same for vacuum conditions, with a constant throat diameter. Separation is predicted to occur when the exit pressure of the nozzle is less than one third of the ambient conditions[7]. The thrust coefficient is set to 0 after which this point occurs.

The validity of the model was determined by testing various known engines to see how well it predicts performance. Appendix A gives the specification of various commercial engines and the predicted values from the model. The predictions are all within 3% for both sea level and vacuum conditions. With this in mind and a fuel choice of Methane[4]. The method of sizing internal engine parameters is as follows.
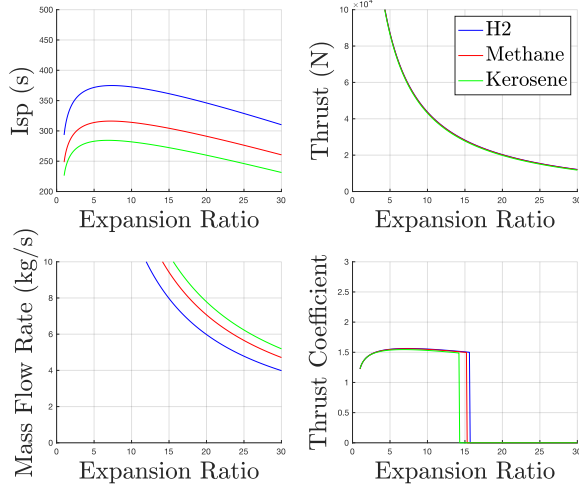
Figure 2: Engine Parameters for varying expansion ratios at a Chamber Pressure of 5.3MPa, Sea Level Ambient Pressure
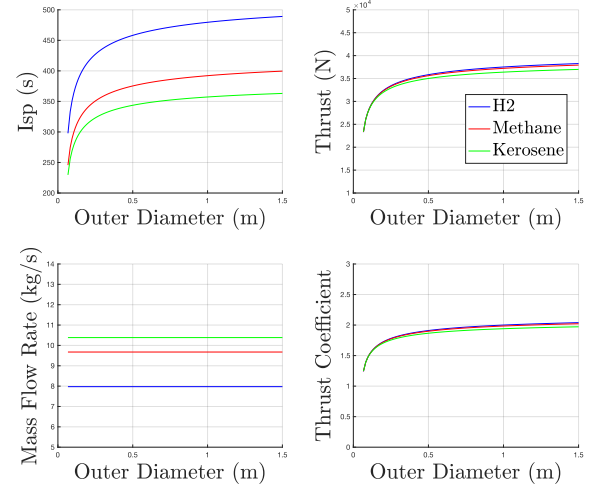

Figure 3: Engine Parameters for varying outer diameters ratios at a Chamber Pressure of 5.3MPa, Vacuum Level Ambient Pressure. Constant throat diameter (6.4cm)

1. Select the number of engines per stage, this is done by determining the wet weights of each stage, then by using the optimal thrust to weight ratio as determined by the ascent trajectory[11]. This also gives the thrust required per engine and also the exit diameter.

2. Determine the chamber pressure and expansion ratio such that separation will almost occur at sea level, this gives the best overall efficiency over the first stage[7].

3. From this the throat area is known, this is constant for both stages. The upper stage expansion ratio is as large as possible, without using a nozzle extension this is limited to around 115[12]. A nozzle extension was ruled as gains are minimal, but there is a significant increase in complexity.

Using this method and figures 2 & 3, the optimal chamber pressure is 5.3MPa, the throat diameter is 6.4cm & the mass flow rate is 9.4kg/s. Table 2 gives other values of interest specific to each stage.

Table 2: Initial Engine Sizing

Stage	Lower	Upper
Area Ratio	15	115
I_{sp} (s)	304	390
Number of Engines	9	1
Thrust (kN)	28.5	33.5

3 Nozzle Design

3.1 Geometry

Rocket engine performance is derived from its ability to convert thermal energy to kinetic energy[7], the nozzles role is to do this in the most efficient manner possible. Nozzle efficiency comes directly from its shape. Early conical nozzles have a constant diverging angle. This has a specific impulse efficiency of around 98%[13]. With an I_{sp} prediction of 300s and a required impulse of 6,000m/s, this two percent loss corresponds directly to a 1% increase in fuel mass fraction from the Tsiolkovsky rocket equation[14]. As payload fractions are typically only 2-3% of total vehicle mass[15], a 1% fuel mass increase could lead to a 33% reduction in useful payload size.

The nozzle consists of three flow regions[7], the first region consists of purely subsonic flow from the combustion chamber to the throat. The second region at the throat contains transonic flow, a mixture of sub and super-sonic flow, and the final, diverging region contains purely supersonic flow. These three regions are illustrated in figure 4.

In the remainder of this section, an analysis of the flow in each region is undertook. A reader not interested in the specifics of methods may skip to the summary section 3.1.4.
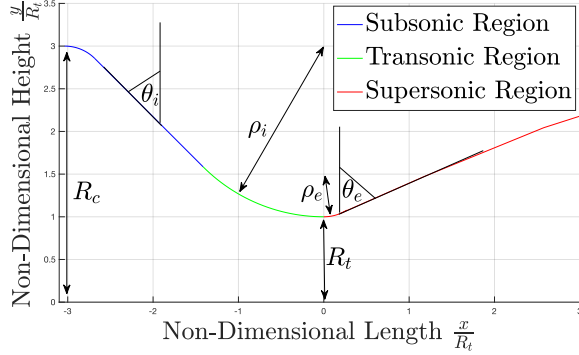
2

Figure 4: Flow Regions of the Nozzle with geometry labelled. Subscript c, i, t & e refer to the combustion chamber, inlet, throat and exit respectively. R refers to a radius, ρ is a radius of curvature and θ is an angle.

3.1.1   Subsonic Contour

The subsonic converging section of the nozzle does not have much of a performance impact[7]. The only requirement is ensuring the converging angle is not too steep, such that flow separation will not occur. Care is also taken to reduce flowfield non-uniformities[16]. Reference [5] gives reasoning for a combustion chamber diameter of 3 times the throat diameter. The inlet angle was set to be $55°$.

3.1.2   Transonic Contour

The transonic region found in the throat of the nozzle starts when the flow is partially sonic to one in which it is fully sonic. The method devised by Sauer[17] is used to solve the flow. It does not have the greatest accuracy, but it is a closed form solution making it ideal for initial analysis[18]. The accuracy is increased significantly by increasing the radius of curvature entering the throat. Sauer showed the following using small perturbation theory.

1. A curve in which the mach number is purely unity[17].

2. A curve in which the flow is also purely supersonic, and the vertical component of velocity is zero at all points[18].

The *second, zero vertical velocity curve*, is taken as the boundary between the transonic throat region and the supersonic diverging region. The reason is twofold, first the flow is purely parallel so is an exact solution to the solid wall boundary condition[18]. Secondly, the Mach lines emanating from the first, purely sonic, curve will

intersect the nozzle wall upstream from the throat point. This makes the solution unsuitable[18].

Equations 2a & 2c describe the velocity distribution and shape of the curve[17].

$$u = \frac{(\gamma + 1)\alpha^2 r}{2} \tag{2a}$$

$$M = u + 1 \tag{2b}$$

$$x = -\frac{(\gamma + 1)\alpha r^2}{8} - \epsilon \tag{2c}$$

α & ϵ are constants given by:

$$\alpha^2 = \frac{2}{(\gamma + 1)\rho_t R_t} \tag{2d}$$

$$\epsilon = -\frac{R_t}{8}\left[\frac{2(\gamma + 1)}{(\rho_t/R_t)}\right]^{1/2} \tag{2e}$$

The solution is considerably more accurate when the ratio of the radius of curvature at the throat to the throat radius is greater than two[18]. In order to keep the nozzle as compact as possible this ratio was set to be 2.

3.1.3   Supersonic Contour

The diverging region is the biggest driver of specific impulse efficiency, this being the losses in I_{sp} when moving from a one-dimensional isentropic case to real three-dimensional flow. This loss in specific impulse efficiency comes from the loss of thrust, but is partially balanced by a slight decrease in mass flow rate[13].

3.1.3.1   Axisymmetric Method of Characteristics

The Method of Characteristics is a technique for solving partial differential equations[19], like those which describe three-dimensional gas flow, into a family of ordinary differential equations in which solutions can be found by integration from known initial conditions[20].

Assume the flow to be irrotational, which when Crocco's theory is applied to the nozzle, is a reasonable assumption[21]. The resulting partial differential equations which describe the gas flow can have the method of characteristics applied to, and as shown in reference [22], the following

ordinary differential equations are found. Equation 3 relates the gradient of the characteristic line and equation 4 fulfills the compatibility requirements along a line.

$$\left(\frac{dr}{dx}\right)_{+/-} = \tan(\theta \pm \mu) \tag{3}$$

$$d\theta \pm \sqrt{M^2 - 1}\frac{dV}{V} = \pm\frac{dr/r}{-(\pm\cot\theta - \sqrt{M^2-1})} \tag{4}$$

The change in signs represents the differences between a left running and a right running characteristic.

3.1.3.2   Local Solution to Flow

Equations 3 & 4 are not analytically solvable, but can instead be solved by numerical analysis. Two finite scheme methods were explored, an inverse marching method and a direct marching method[13]. The direct marching method was selected, as even though it is more computationally intensive, it generally provides more accuracy[13]. A modified Euler predictor, Euler corrected forwards difference scheme[20] is chosen, as opposed to basic finite differences[7]. The convergence found in the corrector algorithm allows high accuracy even when few characteristic lines are used.

Two algorithms were formed as described in Gas Dynamics Vol II[20], one when given two nodes, returns the resulting intersection node. The second, when given one node, returns the interception with the axis of symmetry along the centreline. Both algorithms were tested using case studies to ensure sensible implementation.

3.1.3.3   Global Solution to Flow

The following steps are then used to solve the flow field in the diverging section of the nozzle. Firstly, an initial expansion from the purely supersonic curve determined from the transonic region. The resulting figure 5 shows the characteristic line pattern of initial expansion.

Next, the *kernel* region is formed, this is flow purely determined from the initial expansion and known geometry at the throat. It is created by assuming a throat exit angle. It was decided to keep the the throat exit radius of curvature a constant value of 0.45. This is standard with different sources from literature[16] and industry[23]. The throat exit angle varies as this impacts the final contour nozzle shape. Figure 6 gives an example Kernel region with a throat exit angle of 26 degrees.
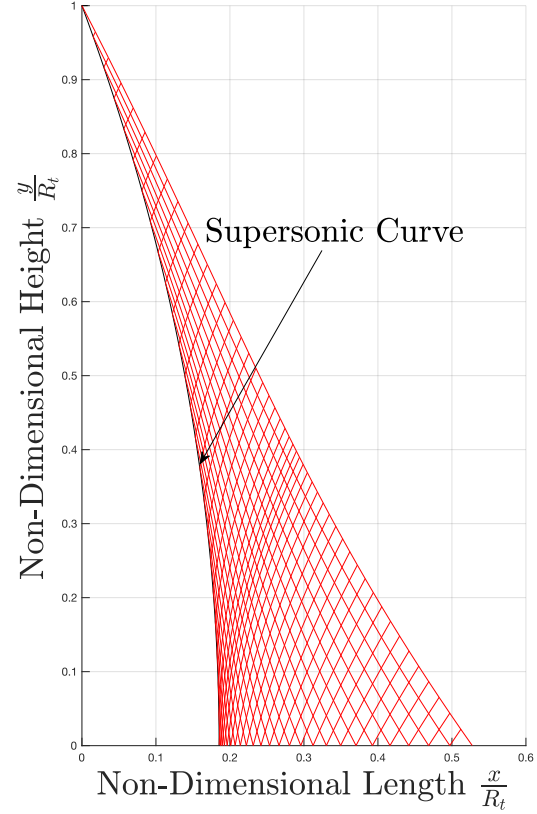

Figure 5: Initial Expansion from Supersonic Line, characteristic lines shown in red

The computational time to work out the initial expansion and kernel region varies with the number of characteristic lines used squared. A sensitivity analysis was run to see how varying the number of lines impacted the average nodal position. Convergence of solutions appears to occur when more than 40 lines are used, figure 7 gives the average nodal position deviation as the fractional difference to 200 lines.

20 characteristic lines are used for generating the kernel and expansion region as further increases had little effect on precision, but significant extra computation time. The result of the study showed convergence with a relatively low number of characteristic lines. This is expected as the Euler corrector algorithm employed iterates until convergence upon a point.

3.1.3.4   Contour Determination

Once the kernel region has been generated, the method described in reference [23] is used to determine the supersonic region nozzle shape. An initial kernel expansion length is given as the input. From this a right-running
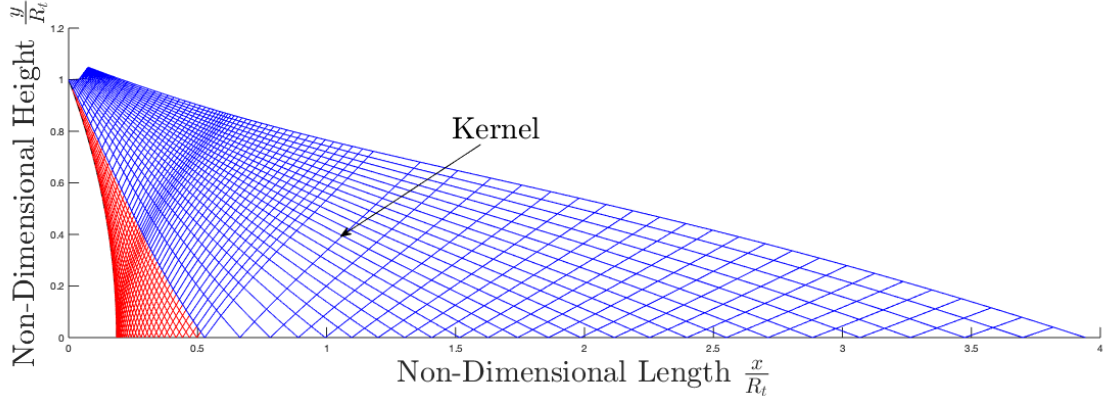
Figure 6: Kernel Region, characteristic lines originating from the throat shape in blue,
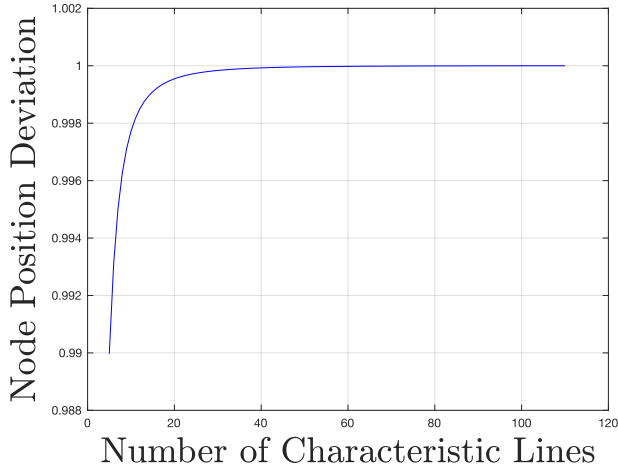

Figure 7: Sensitivity analysis from varying number of characteristic lines

characteristic line can be devised that leads from the centreline, at the required length, cutting through the kernel. From the point in which this line intercepts the edge of the kernel to the end point of the nozzle, Rao specifies a pair of algebraic equations[23]. These are detailed in equations 5a & 5b.

$$C_1 = \frac{V \cos(\theta - \alpha)}{\cos(\alpha)} \tag{5a}$$

$$C_2 = y\rho V^2 \sin^2 \theta \tan(\alpha) \tag{5b}$$

With the known values on the edge of the kernel, constants C_1 & C_2 can be determined, then by increasing y, the Mach number and the flow angle theta can be found along the boundary curve. The length of the curve is then calculated by balancing the total mass flow rate through the throat with the mass flow through the boundary curve

and the curve that cuts through the kernel from the initially specified expansion length. The mass flow rate for a left and right running characteristic is given in equations 6a & 6b.[20][23]

$$\dot{m}_+ = \int (\rho V \frac{\sin(\phi - \theta)}{\sin(\phi)} 2\pi y dy \tag{6a}$$

$$\dot{m}_- = \int (\rho V \frac{\sin(\phi + \theta)}{\cos(\phi)} 2\pi y dy \tag{6b}$$

Finally, the exact nozzle shape is generated using a similar mass flow conservation argument. Balancing the mass flow rate across the left running characteristic line originating at the boundary curve at the current point, to the mass flow rate from the current point on the boundary curve to the remaining length. Figure 8 gives an example of the characteristic lines formed off the boundary curve and the corresponding contour that would be formed.

With the nozzle shape formed, Rao specifies a formula to determine the ambient pressure the contour is designed for, as well as the force produced by the nozzle[23]. Using the area ratio of the generated nozzle, the thrust efficiency and specific impulse efficiency of the contour can also be determined from comparison to the one-dimensional isentropic case. Equation 1d gives the one-dimensional thrust coefficient for a given expansion ratio, equations 7a & 7b[23] gives the thrust the nozzle will produce and the ambient pressure it is designed for.

$$F = \int_C^E (p - p_a + \rho V^2 \frac{\sin(\phi - \theta)\cos(\theta)}{\sin(\phi)} 2\pi y dy \tag{7a}$$

$$\sin(2\theta_E) = \frac{p_e - p_a \cot(\alpha_E)}{\frac{1}{2}\rho_E V_E^2} \tag{7b}$$
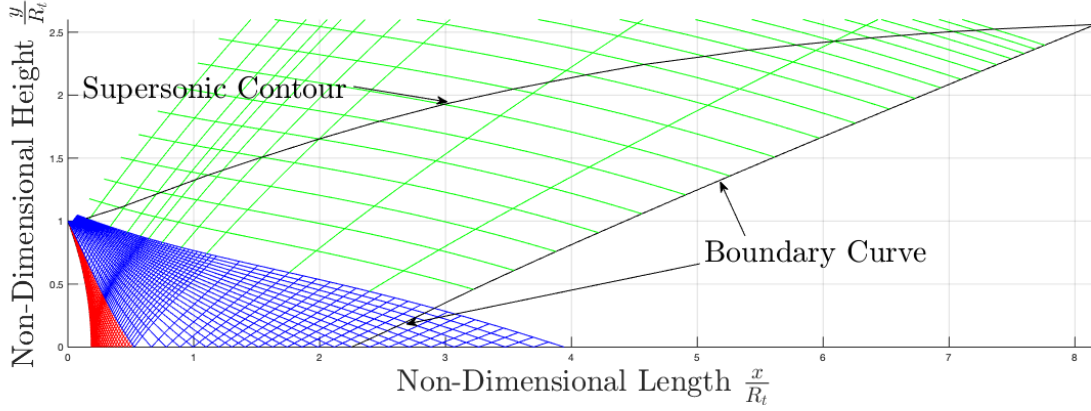
Figure 8: Boundary Curve, green represents characteristic lines originating from the boundary curve

Subscript a refers to ambient conditions, E is the end point on the curve and C is the initial expansion point. The specific impulse efficiency is given by equation 8 [13].

$$\eta_{I_{sp}} = \frac{F}{P_c A_E c_{f_{1D}} \eta_{\dot{m}}}$$ (8)

The mass flow rate efficiency in a 2D axisymmetric flow is 0.9940[13]. Optimal contours for the required expansion ratios as stated in Section 2 are found by changing the throat exit angle, and the the kernel length. The specific impulse efficiency of each combination is then found. Figure 9 shows the result of this study with the non-dimensional length being the total nozzle length as a factor of throat radius.
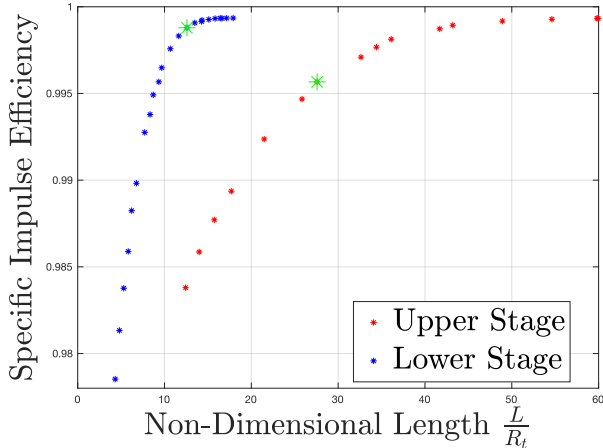

Figure 9: Specific impulse efficiency vs non-dimensional nozzle length for upper (red) and lower (blue) stage expansion ratios

Using Figure 9 design points for both the upper & lower stage nozzles were determined. The design point is that of limiting returns, i.e. the end of quasi-linearity. Table

3 gives the specifications of the nozzles chosen. Figure 10 details the geometry of these nozzles.

Table 3: Specified Nozzle Design Points

	Atmosphere	Vacuum
Non-Dimensional Length	12	29
Specific Impulse Efficiency	0.998	0.996
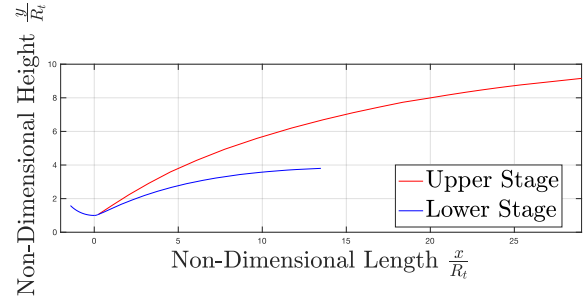
Figure 10: Nozzle shape for the upper (red) and lower (blue) stage nozzles

The 99.8% & 99.6% specific impulse efficiency when applied to the example set out in Section 3.1, gives a payload mass fraction loss of 0.3% and 0.6% respectively. In comparison to the 20% payload mass fraction loss of a non-optimised nozzle this showcases why the analysis is needed.

3.1.4   Nozzle Geometry Summary

An optimal nozzle shape has been determined for the upper and lower stages, these nozzle have a 1.8% and 1.6% increase in efficiency when compared to a conical nozzle. Table 4 summarises the various properties of the subsonic & transonic nozzle portion, lengths are in proportion to

6

throat radii.

Table 4: Non-Dimensional Nozzle Properties in subsonic and transonic regions

Property	R_t	R_c	ρ_i	ρ_e	θ_i (°)
Value	1	3	2	0.5	55

3.2   Cooling

Cooling is essential in rocket nozzles due to the high temperatures of the gases passing through. An expander cycle requires regenerative cooling. From the desire of having as similar a core engine for both upper and lower stages, the amount of heat extracted by any regenerative cooling system must be kept the same. Cooling the larger upper stage nozzle regeneratively would lead to a far higher heat extraction than the lower stage nozzles. The upper stage nozzle is then partially cooled regeneratively and partially cooled radiatively. Radiation cooling is used for three main reasons.

1. Simplicity in design, radiation cooling requires nothing more than a material able to withstand high temperatures.

2. Radiation cooling removes the need for fuel to be wasted with injection of cold fuel into the sides as would be in film cooling[12] or dump cooling[24].

3. Has been demonstrated to be effective on the Falcon 9 upper stage.[3]

In order to design a cooling system, an accurate temperature profile must first be determined. With the known nozzle geometry, the Mach number at any point in the flow can be determined. These numbers are then analysed to work out the heat flux in reference [4]. Figure 11 gives the internal temperature distribution inside the lower stage nozzle.

3.2.1   Regenerative Cooling System Design

The regenerative cooling system design is detailed in reference [4]. It was decided the optimum number of cooling channels was 34, with a diameter of 0.55mm at the throat. The thickness of the wall between the nozzle and the channels is 2mm.

3.2.2   Radiative Cooling System Design

Using the Bartz Equation[24] & and information from reference [4], the approximate values of the conductive heat transfer coefficient at different points in the diverging region of the nozzle have been determined. A one-dimensional heat transfer analysis gives the steady state wall temperature at different points in the nozzle if only radiation cooling was used. Equation 9 gives the relationship required to balance heat transfer into and out of a one dimensional section[24].

$$\epsilon \sigma T_W^4 = h_g(T_r - T_W) \tag{9}$$

Sigma is the Boltzmann constant, epsilon the material emissivity, T_W the wall temperature, h_g is the conductive heat transfer coefficient and T_r is the recovery temperature of the gas which is a function of local wall Mach number and the Prandtl number. Equation 9 is solved from the throat region of the nozzle and the required temperature at each point is shown on figure 12.

Radiation cooling is used after the point the wall temperature drops below 2000K, this is due to material availability. This point occurs at a non-dimensional length of 13.

3.3   Materials & Manufacturing

The nozzle material choices and some manufacturing specifics about the nozzle are detailed below. Broad manufacturing detail is given in more detail in references [4] & [25].

3.3.1   Materials

Typical nozzle material configurations for regeneratively cooled engines consist of an inner & outer liner[24]. The inner liner has the characteristic of very high thermal conductivity, whereas the outer liner has a strength and maximum working temperature requirement. The launcher is also unique in how the first stage is recovered nozzles first *without* retro-propulsion. Retro-propulsion for lower stage recovery has been demonstrated by SpaceX[3] and Blue-Origin[26]. After conferring with the aerothermal team this lead to the requirement that the nozzle must perform in temperatures of 1800K[27]. The upper stage does not have this 'feet first' configuration, but as the nozzle is partially cooled radiatively it must also be able to withstand temperatures above 2000K.

Three different materials will be used in the nozzle. The first material is the inner liner in regions of high heat flux in the inlet and throat section. The second material is a close-out or outer liner material for supporting the inner liner and reducing the chance of catastrophic failure, if the inner-liner were to fail. The third material is used as
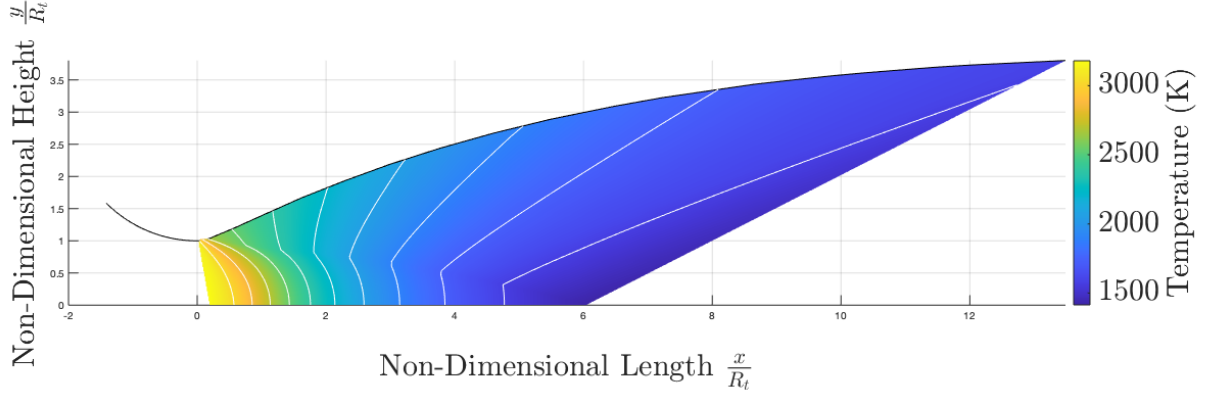
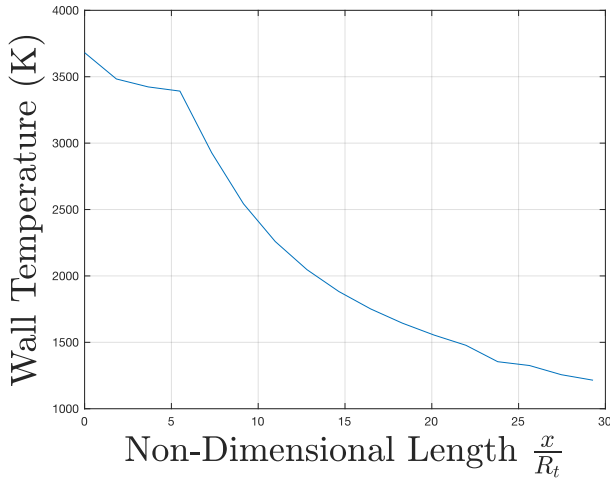Figure 11: Local temperature distribution inside the lower stage nozzle

Figure 12: Wall temperature needed for cooling system using radiation only

a high temperature thermal protection system. It is used from the point in which the lower stage nozzles are no longer covered by the rockets thermal protection systems and also for parts of the upper stage which are cooled radiatively. The material configuration is needed as no one material is capable of meeting all the requirements set out.

CES[28] was used to compare various materials against each other and for the selection of the optimal material for each section. The material choice was limited to only bulk metals and alloys as composites suffered from brittleness and ablation which are not desirable in the nozzle[29]. For the first region a merit function of thermal conductivity against maximum melting point is used, the inner liner is not designed to fulfill structural requirements.
For the outer liner a merit function of melting point against specific strength was used. The outer liner has structural requirements and must also not fail if the inner liner were

to melt.
The final material for the nozzle must be able to withstand temperatures above 2000K without significant performance losses. It must also have good structural strength and a decent thermal conductivity. Materials were limited to those which could stand this heating, and then a merit function is used to maximise thermal conductivity and specific strength. The same material that is used for radiation cooling is used again for parts exposed to entry heating, both sections have very similar requirements and using one material will simplify manufacturing.
Table 5 contains the selected materials and key mechanical and thermal properties. The Ashby plots used to make the material selection are in Appendix B.

Table 5: Nozzle Material Choice and Properties, Thermal Conductivity, Melting Point and Specific Strength

Region	Inner	Outer	High Temp.
Material	Copper	INCONEL 600	Niobium Alloy
TC ($\frac{W}{m}°C$)	380	13	170
M.P. (K)	1350	1539	3680
$\frac{\sigma_y}{\rho}$ ($\frac{kNm}{kg}$)	20.7	97.9	69.9

3.3.2 Manufacturing

Additive manufacturing is used to create the MANTIS engine component by component, references [25] & [6] go into more detail. Using a tri-material configuration for the nozzle will mean the nozzle cannot be produced in one piece. The copper and INCONEL can be manufactured together using a bi-material 3D printer[30]. The Niobium alloy used for parts of the nozzle exposed to high temperatures can be additively manufactured separately[31].

The joining of the two sections is an issue. It was decided to take advantage of the stir welding equipment already

required for the manufacturing of the fuel and oxididser tanks[25]. Niobium and INCONEL 718 can be welded together[32]. INCONEL 600 has very similar properties and so will likely respond in similar ways. A flange-joint[33] could also be used for attachment of the lower nozzle section, however this will lead to a much heavier nozzle.

3.4   Structure & Weight

Nozzles undergo two different types of loads. The first arising from external forces such as wind and atmospheric pressures, the second arising from internal combustion pressures and temperatures[34]. As the copper inner liner is weakened by cooling channels running through it, it cannot withstand the loading. The loads are supported by an externally mounted shell or intermittent retaining bands. Intermittent retaining bands require a continuous shell to some point after the throat in which loads have dropped sufficiently, and then the intermittent band structure can be used. Figure 13 illustrates both methods.

A continuous shell structure is used for a first order mass estimate. Retaining bands would lead to mass savings, but would be hard to quantify in terms of size and strength needed. The highest loading occurs under transient conditions [24]. This requires complicated FEA to quantify which was considered beyond the scope of this report. Approximate thicknesses are chosen for each region. It assumed a copper liner thickness of 4mm. An INCONEL 600 outer liner thickness of 8mm, and a niobium radiative cooling and re-entry protection thickness of 4mm. The ratio of niobium to INCONEL thickness takes into account the reduced loading on outer sections & also the different specific strengths of both materials. Figure 14 shows the breakdown of nozzle mass in each nozzle. The thickness of the copper is taken from the design of the regenerative cooling system.
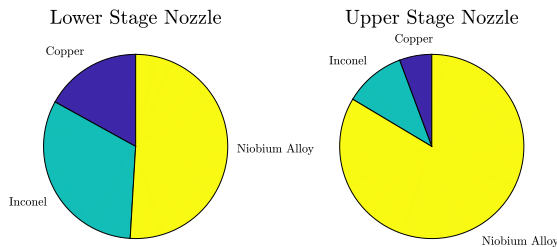

Figure 14: Material Mass Breakdown for Both Nozzles

The niobium alloy dominates the mass. This is expected as it makes up the majority of the nozzle. The first stage total nozzle mass was determined to be 5.4kg and the

second stage nozzle 11.1kg.

3.5   Combustion Chamber Interfacing

Two methods of interfacing were found. These were direct welding of components and a flange joint[33]. The only viable option was to use a flange joint. Welding contains an inherent risk of misalignment which would lead to catastrophic failure if the cooling channels did not align. Welding also has issues with refurbishment and re-use as it would amount to a permanent fixing of the parts together. With a flange joint, the parts can be separated and refurbished individually and then put back together afterwards. This increases average component lifetime, while also following the modular engine design ethos.

3.6   Flange-Joint Structural Analysis

The approach taken for the structural design of a flange joint is to first determine the maximum loading the joint will undergo, typically a safety margin is applied to this as flanges often connect critical components. From the maximum loading requirements the number of fasteners and amount of prestressing needed can be calculated[33]. Due to the the prediction of maximum loading occurring under transient conditions such as engine start and shut off[12], an exact determination is considered beyond the scope of this report.

4   Attitude Control

Attitude control systems are needed to maintain of the rocket. A more detailed control analysis is found in reference [35]. In this section two different attitude control systems and their design are set out. A thrust vector control system is needed for controlling the rocket when the engines are active. A cold gas RCS system is required for control during re-entry and also for reorientation without use of engines.

4.1   TVC Design

One-axis control for some engines and two-axis control for the rest was set out in reference [35]. Different methods of TVC were investigated. A whole engine gimballing system is used because it avoids efficiency losses compared to alternatives like thrust vanes or nozzle only gimballing[12]. The added weight of the whole engine gimballing system
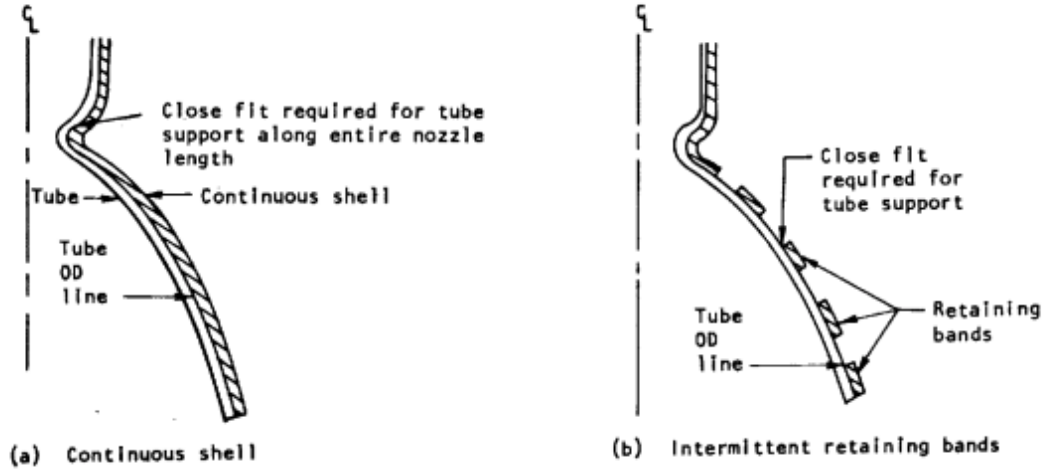
Figure 13: Methods for Structural Support[34]

will be negligible due to the size of the MANTIS engine. Linear actuators are used for both one axis-control and two-axis control. Commercial off the shelf linear actuators were used for both systems, this reduces complexity and also takes advantage of preexisting technologies. A shortlist of actuators were selected from industry leaders MOOG. Table 6 sets out the various properties of the actuators considered.

Table 6: MOOG Actuators & their properties[36]

Characteristic	Size 1a	Size 1b	Size 6a	Size 6b
Length (cm)	28.57	47.62	99.06	163.19
Stroke +/- (cm)	3.17	10.79	9.48	30.12
Weight (kg)	1.81	2.36	199.58	242.67
Power Req (W)	186.42	186.42	29000	29000
Speed (cm/s)	19.05	19.05	12.70	12.70
Max Force (kN)	2.891	2.891	222	222

The vectoring required for each stage is 12 degrees for lower stage nozzles and 30 degrees for upper stage nozzles. The lower stage requirement is based on literature[12]. The actuation required for the second stage is increased because additional vectoring is highly desirable on re-entry. Reference [35] & [37] give additional detail on the vectoring requirements for the upper and lower nozzle. In the rest of this subsection, one axis and two axis TVC will be discussed in more detail and optimal placements given.

4.1.1   One-Axis TVC

One-Axis TVC has a very simple mechanism. Each engine is mounted on a hinge, and a single linear actuator runs from the combustion chamber to the engine thrust plate. By changing the actuator length vectoring will occur.

4.1.2   Two-Axis TVC

Two-axis TVC requires a different mechanism to one-axis TVC. Previous mechanisms patented were examined such as [38],[39] & [40]. These have expired and can be used freely. A similar mechanism as proposed by [39] is used in which two actuators are mounted on gimbals on perpendicular axes which intercept at the engine mount. Vectoring occurs with length changes in either actuator. Actuators will not undergo torsion in this mechanism. A 1D analysis considering only the motion along the axes in which one actuators is perpendicular is desribed in section 4.1.3.

4.1.3   Actuator Placement

Only actuators 1a and 1b are considered for the following analysis as actuators 6a and 6b are too large. The lateral distance is varied and then based on the actuator length, and stroke distance, the maximum vectoring can be determined for each actuator with simple geometry. Figure 15 illustrates how placement impacts the maximum vectoring possible.

In order to meet the 12 degrees of vectoring needed for lower stage engines, actuator 1a can be used with a lateral placement of 16cm. Actuator 1b must be used for the upper stage engine to meet the 33 degrees of vectoring. The lateral placement is 53cm.
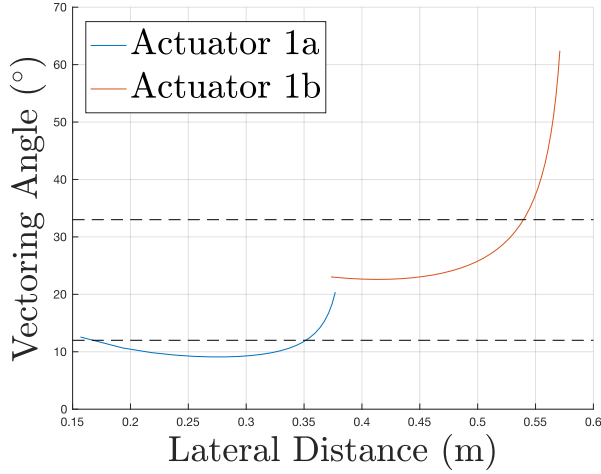
Figure 15: Actuator maximum vectoring angle for a given lateral distance, dashed lines are vectoring requirements for upper (33°) and lower stages (12°)

4.2 RCS System Design

A trade-off study was carried out in comparing helium and nitrogen as a fuel cold gas fuel. A full description is given in reference [6]. To summarise, nitrogen can be stored more densely but has a lower specific impulse. It was opted to use helium as it is already required for tank pressurisation and so the extra storage volume needed is offset to some extent. An RCS thrust of 400N was found to be the required size for control. References [35] & [37] expand upon this decision.

Two different RCS configurations were examined. One in which each individual nozzle has its own pipe connecting it to the tank, and the second in which each RCS block has its own pipe, but each nozzle has its own valve. The second configuration was used as the built in redundancy with individual pipes was weighed to have to much of a mass penalty associated with it. Figure 16 gives the schematic of this RCS system. A common pipe connects the gas tank to each RCS block. Each nozzle then has its own flow regulator valve to allow for individual control.

4.2.1 RCS Sizing

Ideal isentropic relations can be applied to helium in a similar manner to section 2, taking into account its storage temperature[42], and also its chemical properties[43]. The chamber pressure was assumed to be 150 bar as this is the storage in the tank. Due to losses in the pipes the real chamber pressure will be reduced, these losses cannot be quantified at this stage of design. The system will be designed to give a thrust of 450N instead ensuring it
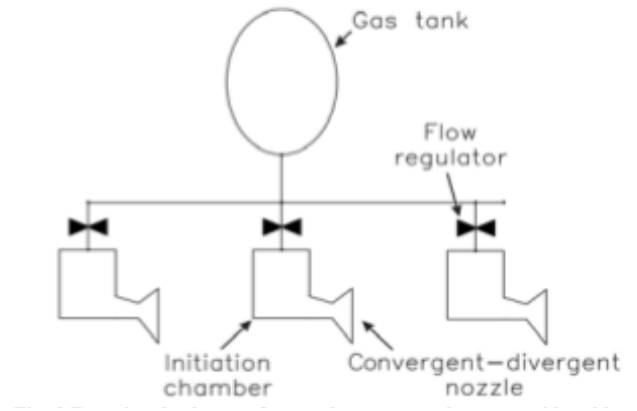

Figure 16: Schematic of the RCS System[41]

meets the minimum requirement. Figure 17 shows the results of this for three different outlet nozzle diameters. It was decided to use an outlet diameter of 3cm as it gave a good specific impulse, but without having a too small of a throat diameter. Table 7 gives the predicted properties from this initial sizing of the RCS system.
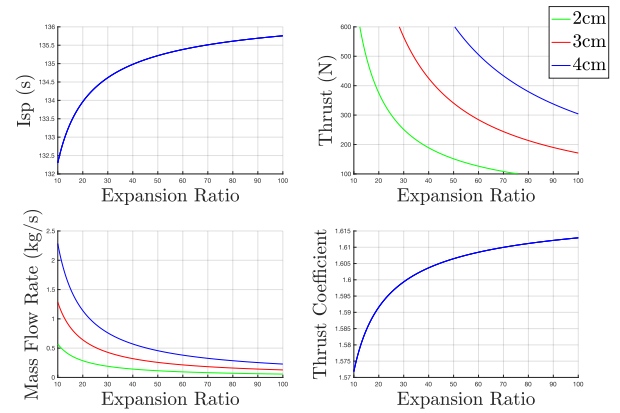

Figure 17: RCS sizing for different outlet diameters

Table 7: RCS Sizing

I_{sp} (s)	$\dot{m}$ (kg/s)	Thrust (N)	Expansion Ratio
135	0.31	450	38

4.2.2 RCS Nozzle Geometry

An exact nozzle geometry can be determined using the same methods in section 3. A similar plot of non dimensional length against specific impulse efficiency is also devised. Table 8 gives the opted for design length and specific impulse efficiency.

Table 8: RCS Design Point

Length (cm)	I_{sp} Efficiency)
7.75	0.9953

From this the geometry of the optimal contour can be found. Appendix C contains the geometry for manufacturer needs.

4.2.3　RCS Valves

Building upon work carried out on design of the plumbing system regarding valves detailed in reference [4], and also from conferring with the controls team[35], minimising the delay between signals being sent and system being activated is needed[35]. Therefore, electrically actuated valves are used. Pneumatic valves though have increased reliability, but the response time is significantly high. Electrically actuated ball valves are used for each nozzle.

5　Discussion

Overall conclusions of the report are given, followed by a brief examination of avenues for future work.

5.1　Conclusions

A method of rocket engine sizing has been developed, it gives a design chamber pressure of 5.3MPa and expansion ratio of 15 and 115 for the lower and upper stage respectively. It predicts an Isp of 304s at sea level for the first stage, and 390s for the upper stage in vacuum.. The underlying model has been tested on many existing engines as detailed in Appendix A, and is found to accurately predict, but to overestimate performance. Performance values have always been conservatively lowered to take this into account.

The nozzle geometry has been accurately determined using Rao's method of optimal thrust[23]. The nozzle length for the lower stage is 51 cm with an exit diameter of 26 cm. Upper stage nozzles have a length of 104 cm and exit diameter of 72 cm. These have an efficiency of 99.8% and 99.6% respectively. A nozzle cooling system has been designed, detailed mainly in reference [4]. A radiation cooling system has been investigated and will start at 40cm after the throat in the upper stage. A tri-material configuration has been outlined for the nozzle consisting of

copper, INCONEL 600 and a Niobium Alloy. The manufacturing required has been considered and potential pitfalls regarding joining have been found. An initial weight estimate gives a nozzle mass of 5.4kg and 11.1kg for the first and second stage respectively. Nozzle-combustion chamber interfaces have been discussed and a flange-joint will be used.

Two attitude control systems have been designed. A TVC system is needed in a one-axis and two-axis configuration for control when the engines are lit. The required control is met with use of COTS linear actuators. A cold gas RCS system is needed for control when the engine is not lit. Nozzles for the RCS system have been designed which produce a thrust of 450N. This is 50N greater than the requirements, but because of pressure losses through the pipe require a conservative system. An electrically actuated ball valve will also be used for precise impulse control.

5.2　Future Work

Further validation of the shape generation method could be carried out using CFD before real world testing takes place. Heat estimations on re-entry and also in the cooling system are preliminary, they are based on empirical equations that overestimate heating, further 3-D analysis will better refine the material requirements needed. Mass estimates are preliminary, a full structural analysis can be carried out to get better nozzle thicknesses. From this a precise weight, and a detailed flange-joint analysis will follow. Nozzle dimensions can then be used for manufacturing. The suitability of welding INCONEL 600 to Niobium alloy needs to be explored. Current information is regarding INCONEL 718. If welding is not viable, different material choices or assembly methods will be needed.

A detailed analysis of two-axis control to give vectoring ranges in all directions would fully characterise the system. From this, a full set of differential equations can be supplied to the controls team to build a more accurate controller. Pressure loss estimations in the RCS system must be determined. From this the margin on the thrust can be reduced and a smaller system designed.

References

[1] JAXA. Piggyback payload. `https://global.jaxa.jp/countdown/f15/overview/sub_payload_e.html#:~:text=A%20piggyback%20payload%20launch%20utilizes,a%20private%20company%20or%20university.`, June.

[2] Rocketdyne. Rs-25 factsheet. `https://www.rocket.com/space/liquid-engines/rs-25-engine`, June 2020.

[3] SpaceX. Spacex merlin engine. `https://www.spacex.com/vehicles/falcon-9/`, June 2020.

[4] Alvaro Fierra Wachtendorff. Regenerative cooling, pressurisation & fluid flow control. Technical report, Imperial College London, 2020.

[5] Tham Ju. Combustion chamber, injector & ignition system design. Technical report, Imperial College London, 2020.

[6] Ramana Sabapathy. Turbomachinery design, throttle control & electrical power system sizing. Technical report, Imperial College London, 2020.

[7] Rocket nozzle performance. In *Rocket Propulsion*, pages 81–133. Cambridge University Press, feb 2019.

[8] Mark Wade. Properties of lox/hydrogen. `http://www.astronautix.com/l/loxlh2.html`, June 2020.

[9] Mark Wade. Properties of lox/methane. `lhttp://www.astronautix.com/l/loxlch4.html`, June 2020.

[10] Mark Wade. Properties of lox/kerosene. `http://www.astronautix.com/l/loxkerosene.html`, June 2020.

[11] Matthew Wong. Ascent trajectory. Technical report, Imperial College London, 2020.

[12] George Sutton. *Rocket propulsion elements*. Wiley, Hoboken, N.J, 2010.

[13] Zucrow Maurice Joseph Zucrow, Joe D. Hoffman. *Gas Dynamics*. John Wiley Sons, 1976.

[14] William Moore. Theory on the motion of rockets. *A Journal of Natural Philosophy, Chemistry and the Arts Vol. XXVII,*, 1810.

[15] James Wertz. *Space mission analysis and design*. Microcosm Kluwer, Torrance, Calif. Dordrecht Boston, 1999.

[16] JERRY L. WAGNER and JOHN D. ANDERSON. Effect of nozzle throat radius of curvature on gasdynamic laser gain. *Journal of Spacecraft and Rockets*, 9(6):471–473, jun 1972.

[17] R. Sauer. General characteristics of the flow through nozzles at near critical speeds. *Deutsche Luftfahrtforchung*, 1947.

[18] Maurice Zucrow. *Gas dynamics, Three-Dimensional Acoustic Waves and Steady Two-Dimensional Transonic Flow*. Krieger Pub. Co, Malabar, Fla, 1985.

[19] Walter A. Strauss. *Partial Differential Equations*. John Wiley Sons Inc, 2007.

[20] Maurice Zucrow. *Gas dynamics, The Method of Characteristics Applied to Steady Two-Dimensional Irrotational Supersonic Flow*. Krieger Pub. Co, Malabar, Fla, 1985.

[21] Paul Bruce. Aircraft aerodynamics course notes. Technical report, Imperial College London, 2019.

[22] WR Sears. High speed aerodynamics and jet propulsion. volume vi. general theory of high speed aerodynamics. Technical report, PRINCETON UNIV NJ, 1954.

[23] G. V. R. RAO. Exhaust nozzle contour for optimum thrust. *Journal of Jet Propulsion*, 28(6):377–382, jun 1958.

[24] Heat transfer in chemical rockets. In *Rocket Propulsion*, pages 177–228. Cambridge University Press, feb 2019.

[25] Hajk Nzsdejan. Supply chain management & infrastructure integration. Technical report, Imperial College London, 2020.

[26] BlueOrigin. New shepherd. `https://www.blueorigin.com/new-shepard/`, 2020.

[27] Francesca Covella. Atmospheric re-entry heating analysis & primary thermal protection system selection, design and sizing. Technical report, Imperial College London, 2020.

[28] GRANTA. Cambridge engineering selector, 2020.

[29] Sp-8124, liquid rocket engine self-cooled combustion chambers. Technical report, NASA, 1995.

[30] Lawrence E. Murr, Edwin Martinez, Krista N. Amato, Sara M. Gaytan, Jennifer Hernandez, Diana A. Ramirez, Patrick W. Shindo, Frank Medina, and Ryan B. Wicker. Fabrication of metal and alloy components by additive manufacturing: Examples of 3d materials science. *Journal of Materials Research and Technology*, 1(1):42–54, apr 2012.

[31] M. Semlitsch, F. Staub, and H. Weber. Titanium-aluminium-niobium alloy, development for biocompatible, high strength surgical implants - titan-aluminium-niob-legierung, entwickelt für körperverträgliche, hochfeste implantate in der chirurgie.

Biomedizinische Technik/Biomedical Engineering, 30(12):334–339, 1985.

[32] Jose Tom Tharappel and Jalumedi Babu. Welding processes for inconel 718- a brief review. *IOP Conference Series: Materials Science and Engineering*, 330:012082, mar 2018.

[33] Engine systems design integration. In *Modern Engineering for Design of Liquid-Propellant Rocket Engines*, pages 345–372. American Institute of Aeronautics and Astronautics, jan 1992.

[34] Sp-8120, liquid rocket engine nozzles. Technical report, NASA, 1976.

[35] Filippos Geragidis. Flight mechanics, navigation & control. Technical report, Imperial College London, 2020.

[36] MOOG. Modular linear electromechanical actuators. `https://www.moog.com/content/dam/moog/literature/Space_Defense/Space_Access_Integrated_Systems/SAIS_Modular_EMA_Rev_0315.pdf`, June 2020.

[37] Rafal Sokolowski. Re-entry vehicle & tps design. Technical report, Imperial College London, 2020.

[38] D. H. T. Huang ETAL. Steerable rocket motor with gimballed nozzle means and cooling means, 1966.

[39] Llyod William Goldberg. Rocket motor thrust control system, 1990.

[40] Rimvykas A Kaminskas. Thrust vector control system for aerospace vehicles, 1966.

[41] Teodor-Viorel Chelaru, S L Valentin Pana, and Adrian Chelaru. The reaction control system based on cold gas for attitude control of a testing launcher. In *2017 8th International Conference on Recent Advances in Space Technologies (RAST)*. IEEE, jun 2017.

[42] Will Horton. Fairing design & cad. Technical report, Imperial College London, 2020.

[43] RSC. Properties of helium. `https://www.rsc.org/periodic-table/element/2/helium`, June 2020.

A   Engine Sizing Model Validation

Various engines in operation and the Raptor engine, which is in development, but uses the same fuel, are used for validation of the model. The method of testing the engine was to use the known thrust and expansion ratio to determine a chamber pressure, from this the specific impulse could be found.

Engine	Real I_{sp} (s)	Predicted I_{sp} (s)
Rutherford SL	311	315
Rutherford Vac	343	346
RS-25 Vac	452.3	458
Raptor SL	330	336
Raptor Vac	383	393
RS-68A Vac	411	421
Vulcain 2 SL	318	325

B   Material Selection Plots

Ashby plots were drawn up to determine nozzle material selection. Figure 18 gives the Ashby plot for the high thermal conductivity region. Figure 19 gives the Ashby plot for the supporting material for the high thermal conductivity region. Figure 20 gives the Ashby plot for the lower stage re-entry protection and radiation cooling section on the upper stage.
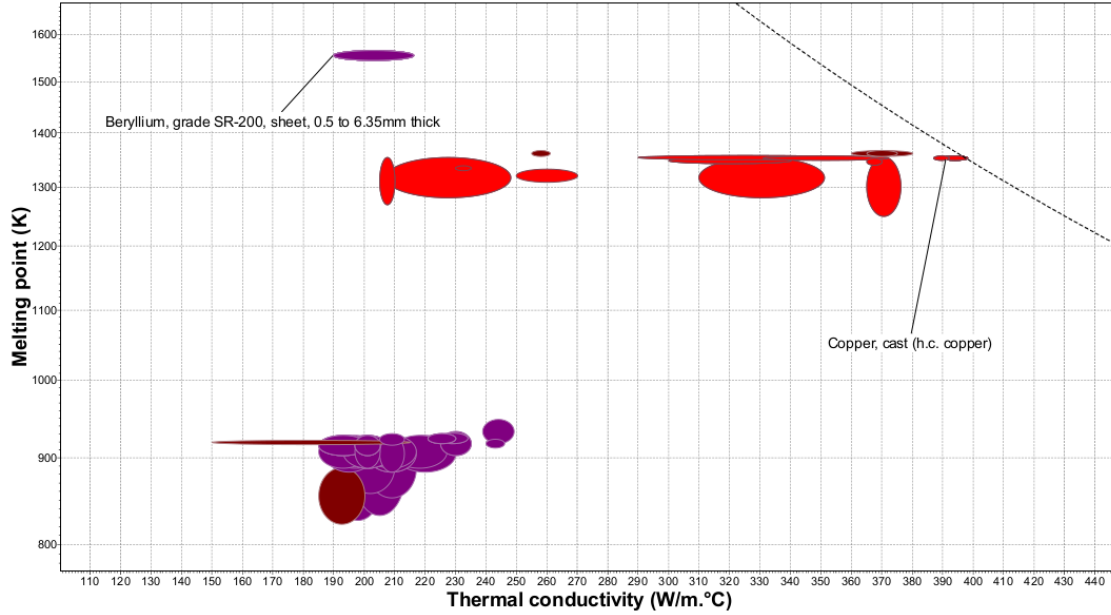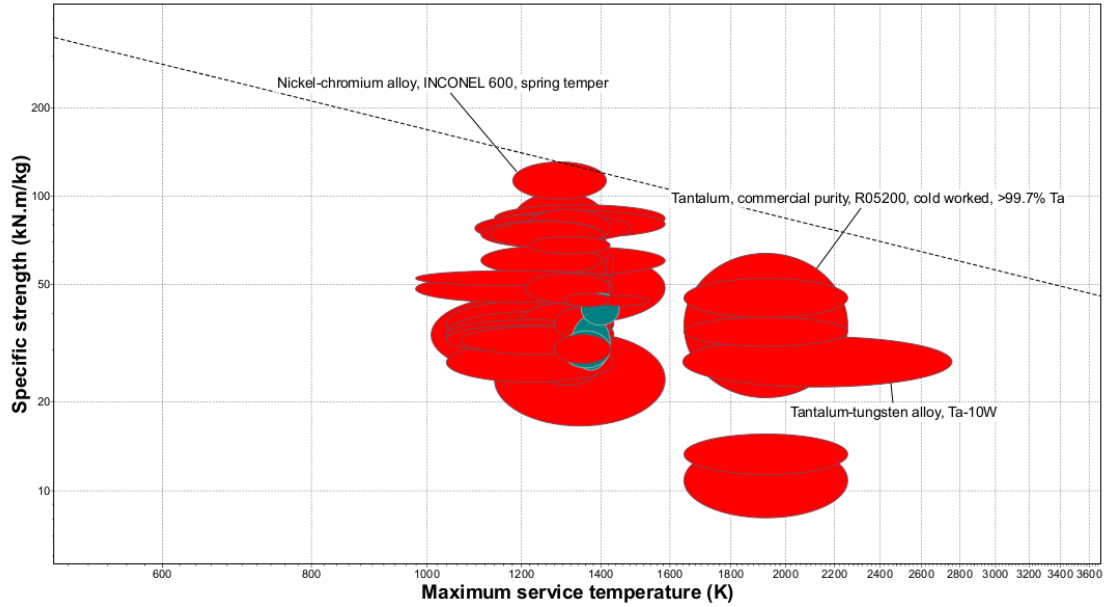

Figure 18: Inner Liner
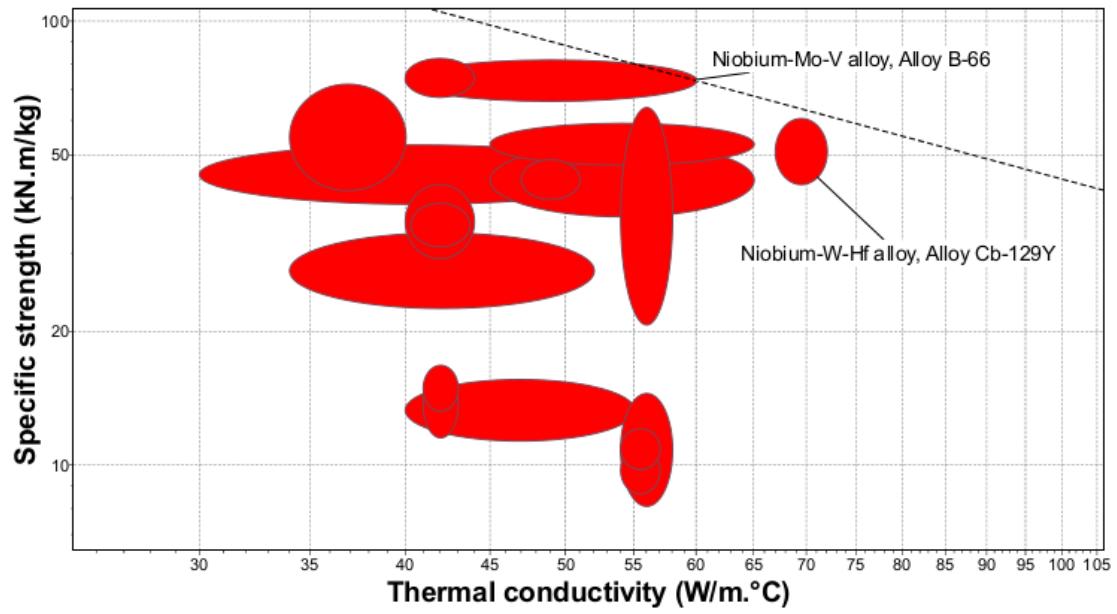

Figure 19: Outer Liner

Figure 20: High Temperature Material

C   RCS Nozzle Geometry
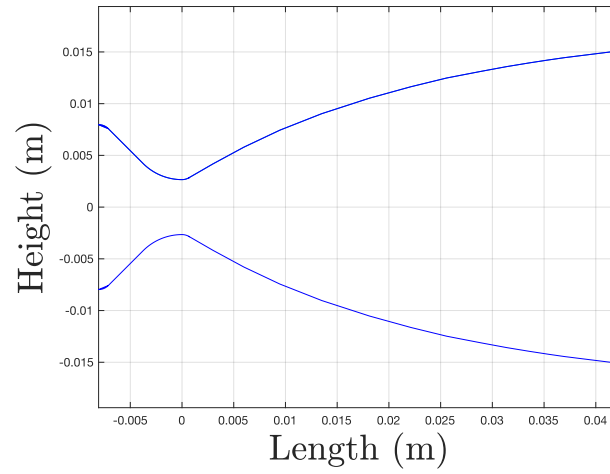
Figure 21 details the exact RCS nozzle geometry as required for manufacture.

Figure 21: RCS Nozzle Geometry